ORIGINAL RESEARCH ARTICLE

Amorphous Intergranular Film Effect on the Texture and Structural Evolution During Cold-Rolling of Nanocrystalline Ni–Zr Alloys

K. VIJAY REDDY, TIMOTHY J. RUPERT, and SNEHANSHU PAL

The presence of amorphous intergranular films (AIFs) in nanocrystalline (NC) metals improves the mechanical properties and thermal stability. However, their influence on the overall deformation behavior of bulk nanostructured materials during the fabrication process is still unexplored. Here, we investigate the texture and defect evolution along with the stress distribution in NC Ni specimens with ordered grain boundaries (GBs), 50 pct AIFs, and 100 pct AIFs during the cold-rolling process. Results from the orientation analysis and texture plots reveal that samples with only traditional ordered GBs show stress-induced grain growth, whereas the presence of AIFs reduces extensive grain rotations and boundary movements. Findings from the atomic stress analysis also indicate tensile residual stress in specimen with amorphous films due to the anisotropic grain elongation without significant grain growth. Further, amorphous films also aid in confinement of dislocations near the surface of the specimens and annihilation of defects in the center grains, thus generating a harder surface and a softer core.

https://doi.org/10.1007/s11661-021-06574-1

I. INTRODUCTION

Nanocrystalline (NC) metallic systems have demonstrated superior mechanical strength[1–4] and enhanced wear resistance.[5–7] These structural improvements are attributed to the high-volume fraction of the grain boundaries (GBs), which are present due to the nanoscale grain size. However, the large GB volume fraction increases the overall energy of the system, thus causing a large driving force for grain growth.[8,9] This energy instability negatively impacts material processing even at low/room temperature (for example, during cold-rolling).[10–14] In order to resolve the issues, the GB character in the NC metallic systems has to be modified through GB engineering such that the interfaces are structurally and energetically stable. One such method of achieving stability of GBs is by solute segregation, through which certain alloying elements are added to the GB to alter its structure, energy, and chemistry.[15–18] Studies have shown that GB segregation could effectively diminish the driving force for grain growth[19] and can induce strengthening.[20] However, solute segregation can also have an adverse effect on the cohesive strength of the GB and can cause embrittlement in metals. For instance, oxygen segregation in NC Al stabilizes the grain structure by inhibiting grain growth; however, it reduces the ductility of the system.[21] Similarly, Ga addition in the GBs of the NC Al specimen decreases the boundary cohesion and eventually leads to embrittlement.[22]

NC metals are also typically brittle compared to their coarse-grained counterparts, limiting their processing capability to large plastic deformations.[3] The structural configuration of the GBs plays an important role in enhancing the damage tolerance of the NC metallic system,[23] marking a potential pathway for improving this common weakness of NC materials. Damage tolerance can be attained through design and control of the fundamental characteristics of the GB, such as the free volume (FV) and the GB energy (GBE). In this perspective, researchers have introduced amorphous complexions, or amorphous intergranular films (AIFs), as interfaces that impart both improved strength and ductility to the material.[24–27] AIFs are phase-like complexions that exist at interfaces with excess FV that aids in the enhancement of atomic diffusion and damage

K. VIJAY REDDY is with the Department of Metallurgical and Materials Engineering, National Institute of Technology Rourkela, Rourkela 769008, India. TIMOTHY J. RUPERT is with the Department of Materials Science and Engineering, University of California, Irvine, CA 92697, USA. SNEHANSHU PAL is with the Department of Metallurgical and Materials Engineering, National Institute of Technology Rourkela and also with Centre for Nanomaterials, National Institute of Technology Rourkela, Rourkela 769008, India. Contact e-mail: snehanshu.pal@gmail.com
Manuscript submitted July 6, 2021; accepted: December 9, 2021.

Published online: 06 January 2022

tolerances.[28] For instance, the presence of Cu–Zr AIFs has been shown to retard the growth of cracks by blunting the crack tip during the tensile and cyclic loading process in NC Cu metallic systems.[27] Moreover, AIFs are also known as efficient point defect sink (both vacancies and interstitials) and can potentially aid in the design of radiation tolerance NC metals.[29] Although the effect of AIFs has been analyzed to determine the strength and ductility enhancement, thermal stability, defect accumulation, and crack propagation, its influence during deformation processing is still unexplored. This gap is important because many methods for fabricating bulk nanostructured materials use severe plastic deformation.

In the present study, we have used molecular dynamics (MD) simulation to analyze the structural and texture evolution of a NC Ni specimen with Ni–Zr AIFs during cold-rolling deformation at 300 K. We have chosen 300 K temperatures as the operating temperature to investigate the influence of rolling on the dislocation behavior, stress distribution, and the grain orientation evolution of the Ni–Zr specimens in the presence of AIFs. Literature studies have also shown that advanced NC Al and Mg systems are also processed through severe plastic deformation, which is a dominant method to develop such materials with desired and precise dimensions.[30,31] In this study, a lower rolling temperature is used to effectively neglect the influence of temperature on the deformation behavior and to avoid dynamic recrystallization process. Cold-rolling of pure NC metals has already been studied for various systems using experimental techniques and the structural transformation, defect evolution, and texture has been analyzed.[11,32,33] However, the effect of AIFs on deformation behavior and the overall texture evolution during the cold-rolling process is yet to be explored. Literature studies have shown that MD simulation is an efficient tool in mimicking the orientation development, the evolution of defects, and analyzing the stress distribution during the rolling deformation.[34–38] Here, we have performed various analyses such as grain orientation distribution, orientation scatter, stress distribution, and dislocation analysis to comprehend the deformation behavior during the rolling process. Overall, the findings highlight that AIFs restrict interfacial movement and grain growth compared to the ordered GBs. Moreover, the dislocation annihilation due to the AIF aids in the formation of elongated grains with lower stress and defects after the rolling process. In the subsequent sections, we have elaborated on the computational methodology of the cold-rolling process and discussed the findings obtained through the analysis.

II. COMPUTATIONAL METHODS

A. *Specimen Construction and Specimen-Rollers Model Setup*

First, we have designed a NC Ni specimen having hexagonal grains (16 grains with an average grain size of ~ 9 nm) with overall dimensions of 30 × 15 × 20 nm using the Atomsk platform.[39] We have specifically considered hexagonal-shaped grains to avoid sharp edges with high-stress concentrations and to maintain a uniform spatial distribution of the grains within the specimen. After specimen construction, we have performed energy minimization using the conjugate gradient method to obtain the static stability of the atoms.[40] To prepare the NC Ni specimen with AIFs, we have first identified the GB atoms using polyhedral template matching, PTM[41] and then removed them from the specimen. Simultaneously, we have created a $Ni_{64}Zr_{36}$ metallic glass (MG) specimen having similar dimensions to that of the NC Ni specimen. After that, we have merged both the specimens, *i.e.*, NC Ni without GB atoms, and the Ni–Zr MG specimen and removed the MG phase from the grain interior, thus resulting in a specimen with Ni grains and Ni–Zr AIFs as an interfacial phase or complexion. The thickness of the AIFs is taken as 1.3 nm, and the simulation process has been performed using the LAMMPS package.[40] For a comparative study, we have considered (1) a pure NC Ni specimen with ordered GBs, (2) a specimen having 50 pct AIFs and 50 pct ordered GBs, and (3) a specimen having 100 pct AIFs as interface structures (refer Figures 1a through c). Before the initiation of the cold-rolling, we have equilibrated the specimens by heating them up to 900 K, holding them at 900 K for 50 ps, and then cooling to 300 K at a cooling rate of 5 k ps^{-1} (cooling from 900 K to 300 K in 120 ps). The equilibration process has been carried out under the NPT ensemble (constant pressure and temperature), and the temperature is controlled using the Nosé–Hoover thermostat.[42] The boundary conditions used are periodic in all three directions during the equilibration procedure. Once the equilibration of the specimens is completed, they are merged with three sets of rigid rollers to generate the specimen-roller setup (Figure 1(d)). The diameter of the rollers is taken as 14 nm, and the rollers span the simulation cell along the *Z*-direction. The first roller set is positioned such that the thickness reduction percent is 8 pct of the initial specimen, whereas the second and third roller set has a thickness reduction percent of 20 and 30 pct, respectively. We note that the thickness reduction for the *n*th roller set is calculated for the NC specimen that has traversed through the $(n-1)$th roller set. The upper rollers rotate in an anti-clockwise direction, whereas the lower rollers rotate in the clockwise direction. After the specimen-roller model setup is created, the model is again equilibrated at 300 K (cold-rolling condition) under NVE ensemble, and the temperature is controlled using Nosé–Hoover thermostat.[42] The *X*-axis is specified as the rolling direction (RD), *Y*-axis as the normal direction (ND), and the *Z*-axis as the transverse direction (TD). The boundary conditions along the RD are changed to non-periodic and shrink-wrapped during the cold-rolling process, and the time step is considered to be 2 fs for the entire simulation run.

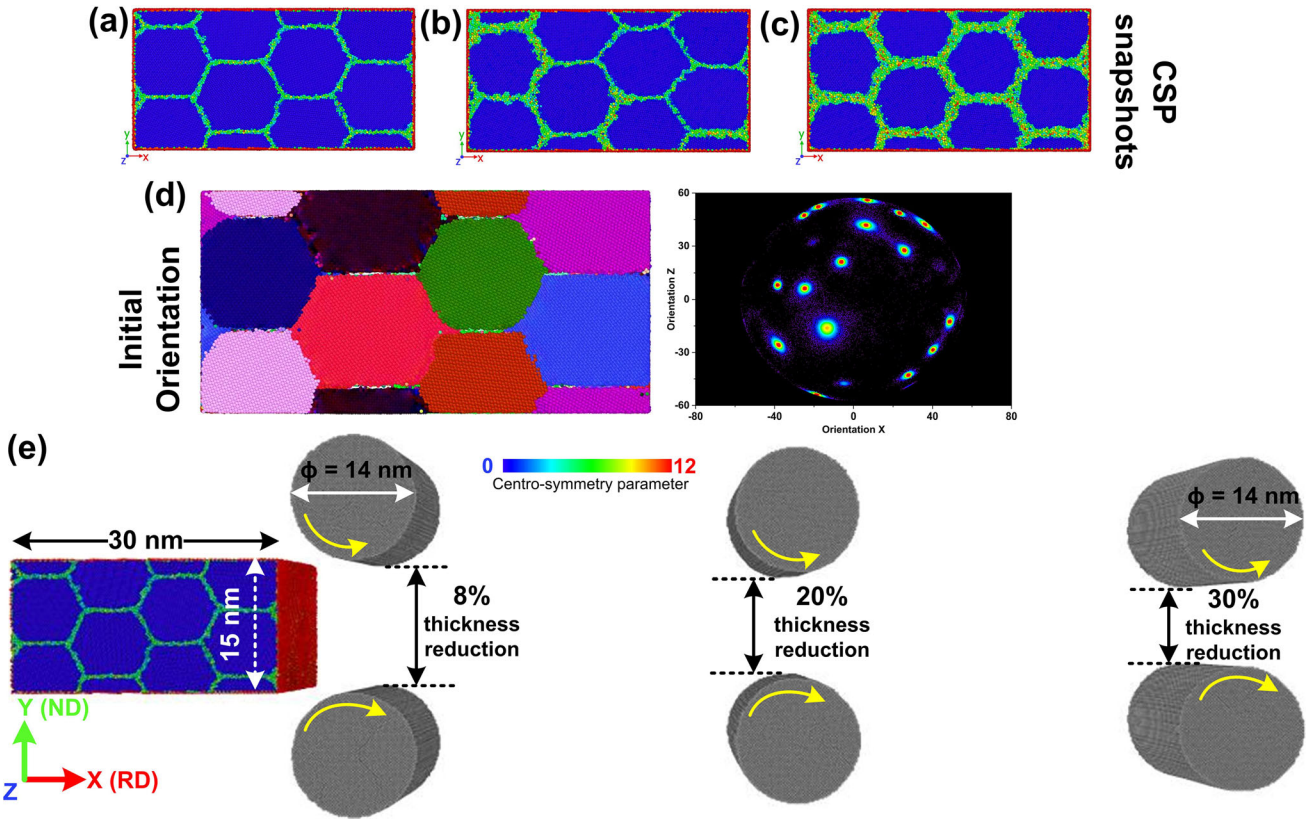

Fig. 1—(*a* through *c*) Atomic centro-symmetry parameter (CSP) snapshot of the specimen with ordered GBs, 50 pct AIF, and 100 pct AIF, respectively, (*d*) Atomic orientation snapshot along with the orientation plot of the initial unrolled NC Ni specimen, and (*e*) NC specimen along with the three set of rollers for the nano-rolling process. The reduction percentage during the passing of each roller is specified. Here, RD indicates rolling direction, TD indicates transverse direction, and ND indicates the normal direction.

B. *Evaluation of Lattice Orientation*

For identifying any alterations in the orientation of the grains, we have implemented a Python-based analysis algorithm in accordance with PTM-identification of crystal orientation that determines the alteration in the local lattice orientation during the rolling process.[41] The orientation analysis process is implemented in the OVITO package.[43] In order to store the information of the calculated lattice orientation, we have used the quaternion ($\boldsymbol{q}$) values, which is a set of vector and scalar elements $[q_0, q_1, q_2, q_3]$.[44]. The first term q_0 is the scalar term and the next three terms, q_1, q_2, q_3 represent the vector terms. During the cold-rolling process, the compressive/shear deformation leads to the change in orientation through grain rotation and the information, which is stored in the matrix $[q_0, q_1, q_2, q_3]$ can be associated with the alteration of the angle of rotation and the rotation axis through a unit vector, $\boldsymbol{\xi}$.[44] The rotation angle (ω) is signified by the scalar term of the quaternion, q_0, which is represented as $\cos\left(\frac{\omega}{2}\right)$ and rotational axis (ξ_i) is signified by the vector terms, q_1, q_2, q_3, and is represented through $\sin\left(\frac{\omega}{2}\right)$. In the current investigation, we have determined the change in the lattice orientation (through the angle of rotation,ω) of the grains by using the first term,q_0 of the computed quaternion matrix. After that, the calculated value of ω is implemented to obtain the rotational axis (ξ_i) using the vector terms, q_1, q_2, q_3. A similar methodology for determining the alteration in grain orientations during the rolling process has been implemented in various literature studies.[14,34]

III. RESULTS AND DISCUSSION

Figure 2 shows the distribution of grain orientation angle along with the orientation snapshot for the unrolled and the rolled specimens (with and without AIFs). The unrolled NC Ni specimen shows a uniform distribution ranging from ~ 20 to 60 deg. The initial orientation angle between the grains has been predefined during the preparation of the NC specimen. Upon cold-rolling of the specimen with ordered GBs, it is found that the grain orientation angle distribution changes non-uniformly with two larger peaks near the ~ 40 to 45 deg range and a smaller peak near the ~ 60 deg (as shown in Figure 2). It is observed that the gray region (~ 40 to 45-deg range) constitutes almost 30 pct of the atomic fraction. This distribution is attributed to stress-induced grain growth during rolling in few grains (colored with red, green, and purple, based on quaternion value), leading to a bimodal-like grain distribution (refer to the inset of the rolled specimen with ordered GBs in Figure 2). Experimental findings have also shown similar orientation angle distribution trends

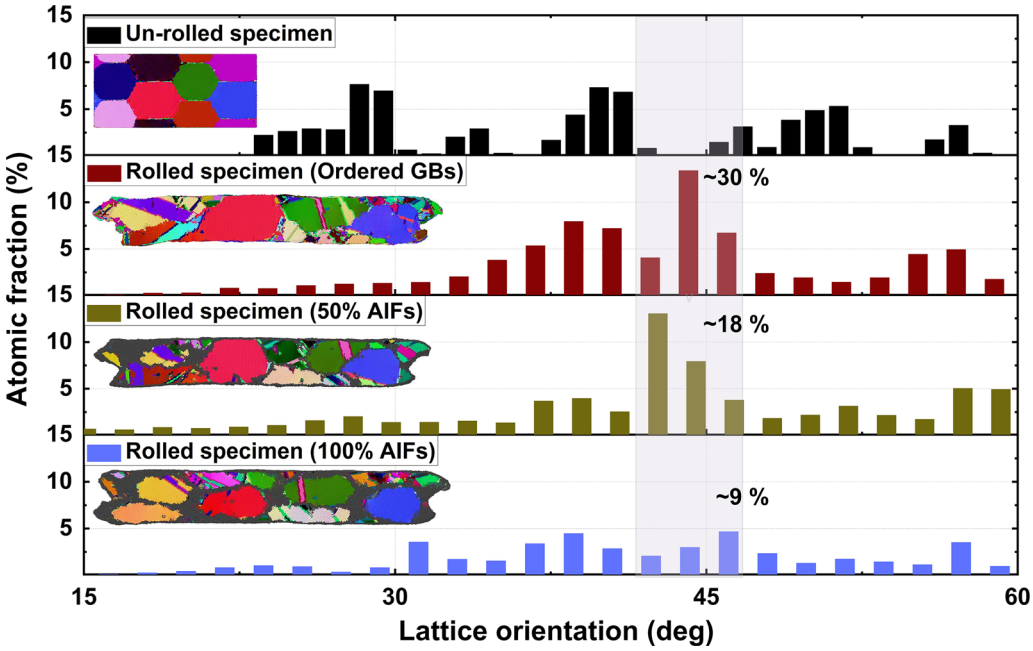

Fig. 2—Grain orientation angle distribution for the unrolled and the rolled specimens (with ordered GBs, 50 pct AIF, and 100 pct AIF), (inset) shows the atomic snapshots colored with respect to the atomic orientations (Color figure online).

during the recrystallization process after Ni specimen rolling.[45] However, the inclusion of 50 pct AIF as interface in the NC specimen substantially reduces the intensity of larger peaks compared with the distribution of rolled specimens with ordered GBs. In this case, plastic strain is mostly absorbed or accumulated by the AIFs and the deformation is partially controlled by the formation of twins. Hence, we can observe a slight increase in the atomic fraction at 60 deg lattice orientation when compared to the unrolled specimen in Figure 2. The non-uniformity in the distribution is still evident when we compare it to the initial unrolled specimen as the grains without AIF as the interface can still grow in size (refer to the inset of the rolled specimen with 50 pct AIF in Figure 2). For the rolled specimen with 100 pct AIF, it is seen that the grain orientation angle distribution is uniform along with lowered peak intensity. Moreover, the grain growth is restricted due to the presence of AIF. However, their shapes have been distorted and elongated along the RD, as it can be roughly assessed by the orientation snapshot (inset). Apart from the distortion and grain elongation, specimen with 100 pct AIF undergoes plastic deformation through the formation of defects such as twins and stacking faults (SFs). The presence of twins and defects inside the elongated grains leads to a different orientation due to which, the overall distribution of the lattice orientation of the specimen becomes uniform with lower peak intensity. However, most of the grains retain their orientation without grain growth or grain refinement in case of 100 pct AIF even after the rolling process as shown through the atomic snapshot (inset in Figure 2). Detailed quantitative analysis on the change in the orientation angle of grains in the presence of AIF is presented in the subsequent sections.

We have analyzed the structural development and the texture evolution of the NC Ni specimen with ordered GBs after each roller pass and presented it in Figure 3. The initial texture shows concentrated and distinguished spots for each of the 16 grains representing their orientation along the RD and TD (refer Figure 3(a)). Upon passing through the first set of rollers, the compressive deformation causes the formation of SFs and distortion in the grain structure in a few of the grains without drastic alteration in their orientation. The formation of SFs induces imperfections inside the perfect lattice of the grain and disturbs the alignment of the atomic planes. This process leads to dissemination/spreading in the texture plot indicating a slight distortion in the orientation of the grains (refer Figure 3(b)). After the specimen traverses through the second set of rollers (~ 20 pct thickness reduction), the severe plastic deformation is accommodated through SFs, twins, and low-angle GBs (LAGBs). These structural modifications have also resulted in the grain refinement process near the surface regions observed in the atomic snapshot in Figure 3(c). Simultaneously, the texture also shows an RD-splitting, *i.e.*, the orientation's shift toward the end along the RD, although few spots have retained their initial positions. This corresponds to the centrally located grains (colored in red, green, and violet based on quaternion value) that do not undergo drastic orientation alteration. On further cold-rolling the specimen (~ 30 pct thickness reduction on the specimen rolled through the second roller set), these grains are found to be enlarged as shown in the orientation snapshot (refer Figure 3(d)).

On the other hand, we have also analyzed the structural and texture evolution of the NC Ni specimen with 100 pct AIF after each roller pass in Figure 4. It is

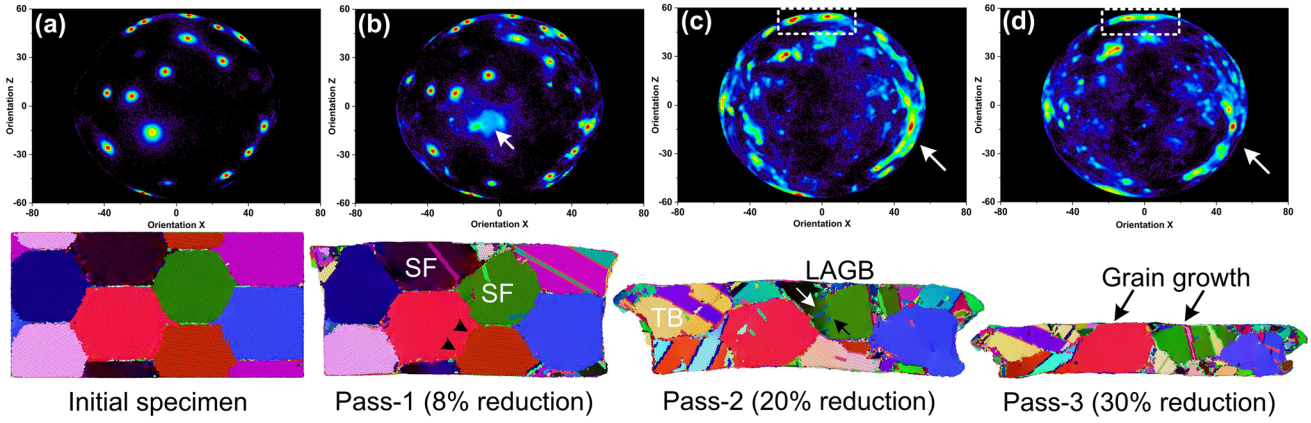

Fig. 3—Orientation plot along with the atomic snapshot for the (*a*) initial unrolled specimen with ordered GBs and the rolled specimens after traversing (*b*) roller set-1, (*c*) roller set-2, and (*d*) roller set-3. Here, LAGB indicates low-angle grain boundaries; dotted boxes show that the orientation of the spots did not alter after the rolling process.

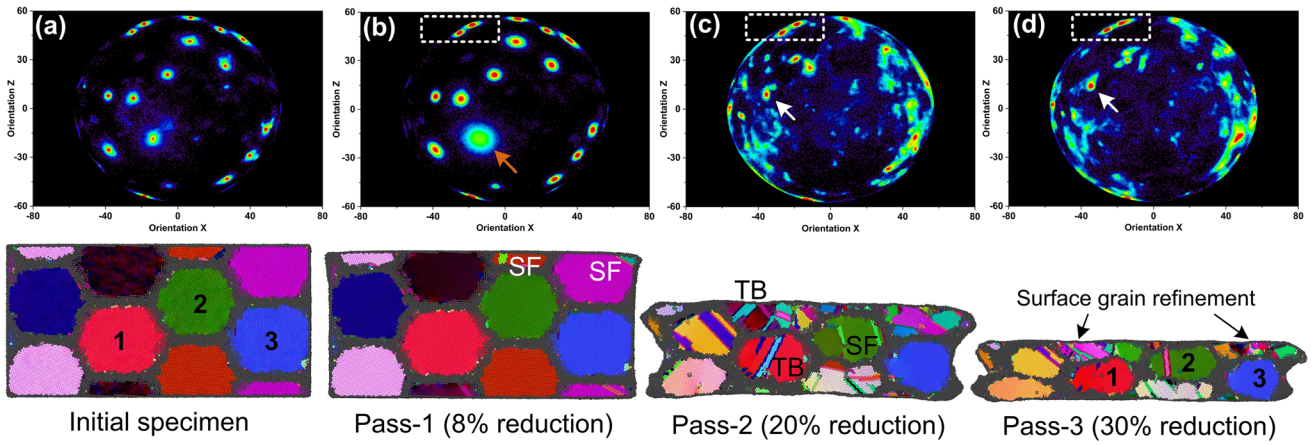

Fig. 4—Orientation plot along with the atomic snapshot for the: (*a*) initial unrolled specimen with 100 pct AIF and the rolled specimens with AIF after traversing (*b*) roller set-1, (*c*) roller set-2, and (*d*) roller set-3. Here, SB and TB indicate SFs and twin boundaries, respectively; dotted boxes show that the orientation of the spots did not alter after the rolling process.

to be noted that we have removed the atomic orientations of the AIF atoms in the texture plot to reduce the noise, as the prime motive is to understand the evolution of grain orientation in the presence of AIFs. Similar to the previous case, we have observed concentrated and distinguished spots representing the orientation for each of the grains before cold-rolling (refer to Figure 4(a)). Upon passing through the first set of rollers, we observe a slight dispersion in the texture plot (indicated through arrow) due to the formation of SFs in the upper region of the specimen; however, the hexagonal grain structure is intact due to the presence of AIFs (refer Figure 4(b)). On further deformation, it is seen that the plastic deformation is accrued through twinning and grain segmentation as the presence of AIF does not allow interfacial movement or grain growth. Even though we observe RD-splitting, a higher number of grains have retained their initial orientation, as depicted through the texture plot in Figures 4(c) and (d). Whereas, few other grains (spots on the texture plot) have shown a minimum shift from their original position, indicating a minimal grain rotation (refer to Figure 4(d)). For a better understanding, we have compared the extent of grain rotation in the specimens with ordered GBs and 100 pct AIFs by calculating the difference in the grain orientation for the initial (unrolled) and final (after rolling) conditions (refer Figure 5). Also, we have set a cut-off angle to 5 deg for the minimum change in orientation angle because angles lower than 5 deg are in general responsible for the formation of sub-GBs.[46] By considering a 5 deg as cut-off (*i.e.*, orientation angle difference), we can assume that the grain rotation after the rolling process is minimal and no new GBs (either LAGBs or HAGBs) have been formed. It can be observed that most of the grains in the specimen with ordered GBs deviate from the initial orientation to a larger extent, having a change in orientation angle difference greater than 10 deg (refer Figure 5(a)). As previously discussed, the morphology of the grains in the specimen with ordered GBs undergoes drastic alterations during the rolling process as both grain growth and grain refinement are observed. Hence, we have used error bars to indicate the variation in the change in orientation due to the refinement of grains. It

can be seen that few grains, mainly on the surface region, have shown more significant variation in the change in orientation angle due to the segmentation/refinement of grains (refer Figure 5(a)). On the other hand, specimen with 100 pct AIFs show minimal alteration in the change in orientation angle as most of the grains are below the cut-off angle (refer Figure 5(b)). Moreover, the near-surface grains (G-3, 5, 7, and 9) with higher change in orientation do not show large error bars as the refinement of grains is caused primarily due to the generation of twins. The analysis clearly indicates that the specimen with AIFs can restrict the grain rotation or texture in the specimen. Such anisotropic nature in the NC grains can enhance the mechanical properties without much alteration in the texture.[47] For better visualization, we have provided the surface profile of the rolled specimens (both ordered GBs and 100 pct AIFs) in the Supplementary Material.

Figure 6(a) shows the atomic stress distribution along RD for the specimen with ordered GBs after traversing through each roller set. It is to be noted that the stress distribution in each grain is not uniform and there are localized tension and compressive regions along the specimen thickness and transverse section. This is the reason due to which we have shown the atomic stress distribution with respect to the atomic fraction, and not with respect to the specimen region. It is observed that cold-rolling through the first set of rollers induces compressive residual stress to most of the atoms, as the peak shifts slightly toward the compressive stress zone. The atomic stress snapshot (inset) also indicates negative stress regions in the specimen along with very few positive stress regions. Furthermore, the average stress along the RD for both the GB network and the grain interior is negative, as observed in Figure 6(b). After passing through the second set of rollers, we observe a sharp decrease in the peak value and a simultaneous increase in the higher compressive stress values, which indicates an increase in the residual compressive stress in the specimen. This can be validated through the atomic snapshot (inset) that shows high concentrated negative stress regions in the specimen.

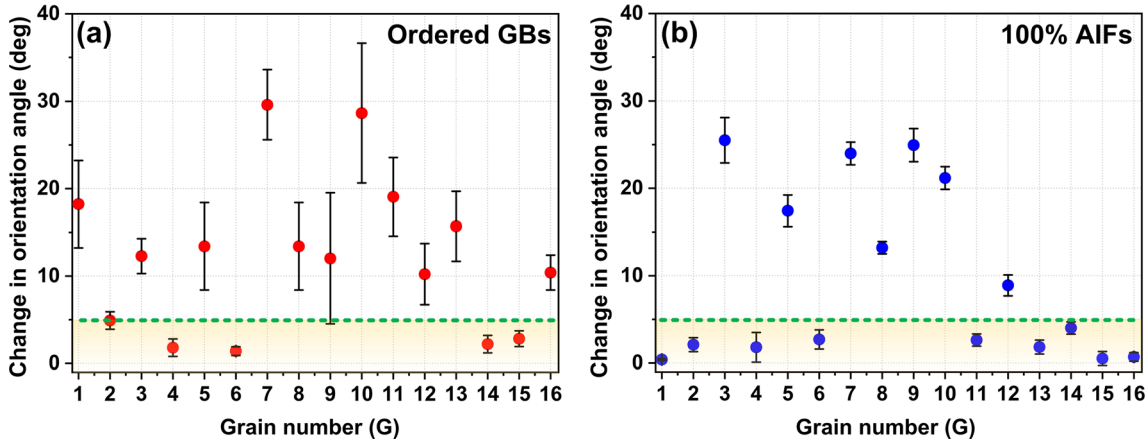

Fig. 5—Plot illustrating the difference in the orientation angle for the unrolled and the final rolled specimens: (*a*) with ordered GBs, and (*b*) with 100 pct AIF. Green dotted line indicates the cut-off for change in orientation angle that is considered significant (Color figure online).

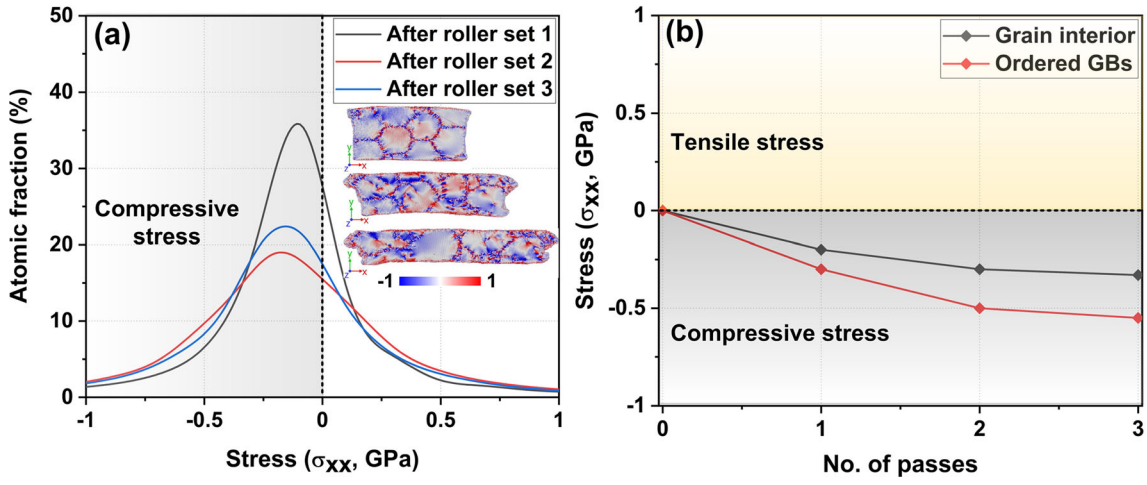

Fig. 6—(*a*) Atomic fraction *vs.* stress plot showing the distribution of stress for the specimen with ordered GBs after passing through each roller set, and (*b*) plot showing the average stress along the RD after passing through each roller set.

However, it is found that the rise in the average compressive stress in the grain interior of the specimen after rolling through the second roller set is minimal (refer to Figure 6(b)). In contrast, the GB network shows a larger average compressive stress value after passing through the second and third set of rollers, which might be responsible for the grain fragmentation and formation of sub-GBs. The finding is consistent with experimental studies, where surface rolling techniques are implemented to cause the formation of nanostructured grains.[48] In the case of the specimen with 100 pct AIF, we have found similar stress distribution after passing through the first set of rollers; however, a small spike at higher stress values (both positive and negative stress) is observed (refer Figure 7(a)). But, contrary to the previous case, we have found that the average stress in the grain interior is positive (tensile stress), whereas the AIF region shows a negative (compressive) stress, as shown in Figure 7(b). As the specimen traverses along the second and third set of rollers, the increase in the magnitude of the compressive stress in the AIF is minimal when compared with the specimen with ordered GBs, which can be attributed to uniform distribution of stress (and inhibition of stress localization) along the AIF network during the rolling. Moreover, the average positive stress (tensile stress) along the RD increases in the grain interior due to the anisotropic grain elongation without significant grain growth.

Figure 8(a) illustrates the dislocation density distribution along the ND of the specimens (for ordered GBs, 50 pct AIFs, and 100 pct AIFs) after the cold-rolling process. It is seen that the specimen with ordered GBs shows the highest and uniform dislocation density

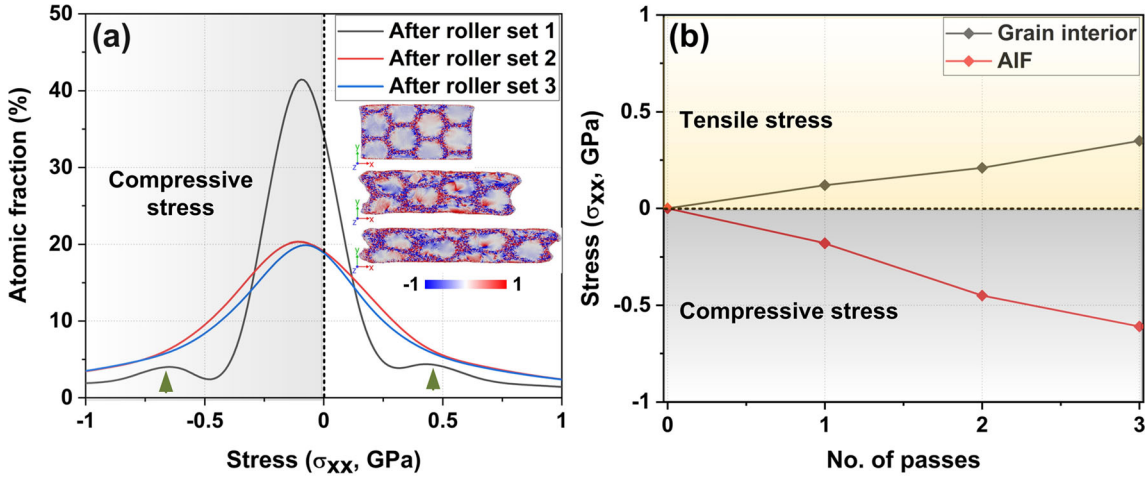

Fig. 7—(*a*) Atomic fraction *vs.* stress plot showing the distribution of stress for the specimen with 100 pct AIF after passing through each roller set, (inset) atomic snapshot of the rolled specimens colored by their local atomic stress along the RD (*x*-axis) and (*b*) plot showing the average stress along the RD after passing through each roller set.

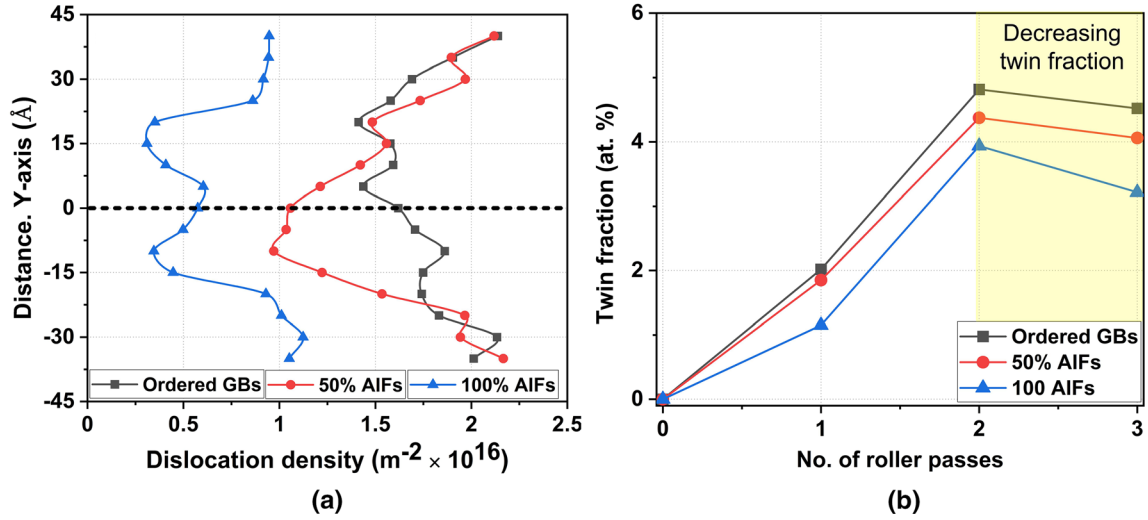

Fig. 8—(*a*) Plot illustrating the dislocation density distribution along the ND (*y*-axis) of the specimen for the three specimen (*i.e.*, ordered GBs, 50 pct AIF, and 100 pct AIF), and (*b*) plot showing the variation in the twin boundary fraction after passing through each roller set for the three specimens (*i.e.*, ordered GBs, 50 pct AIF, and 100 pct AIF).

throughout the thickness of the specimen. The specimen with 50 pct AIFs also shows similar dislocation density distribution near the surface regions; in contrast, the central region has a lower density when compared to the specimen with ordered GB (refer Figure 8(a)). This indicates that the presence of AIF absorbs the stress and reduces the prospect of dislocation nucleation. The phenomenon is clearly observed in the specimen with 100 pct AIF, where the overall dislocation density is the lowest (refer Figure 8(a)). Moreover, a comparatively higher dislocation density is accumulated near the surface region, which is deformed to a greater extent. The reason behind higher plastic deformation at the surface of the specimen is due to its close proximity to the rollers. The rollers induce both compressive and shear forces on the specimen during the rolling process. And as the specimen surface is nearest to the rollers, the magnitude of shear force is more at the surface as compared to the center of the specimen. Hence, a comparatively higher plastic deformation occurs at the surface when compared to the center of the specimen.[49] In case of ordered GBs, it is observed that the dislocation density is same along the depth for most of the region (1.5 to 1.7 $\times$ 10^{16} m^{-2}) except near the surfaces where it increases gradually to a maximum value. On comparison with that of the specimen with AIFs (50 and 100 pct AIF), there is an abrupt decrease in the dislocation density in the interior grains indicating that a few grains in the specimen have almost no dislocations (also shown through dislocation snapshots in Figure 9). Such a non-uniform dislocation density distribution due to AIF can impart stress-induced strength at the surface and a softer core at the central region of the specimen. Figure 8(b) shows the variation of the twin boundary fraction in the specimens (for ordered GBs, 50 pct AIF, and 100 pct AIF) after each roller set. It is found that the TB fraction rises with an increase in the roller set till the second set, after which there is a slight reduction in the twin fraction for the three specimens (refer to Figure 8(b)). We have also illustrated the atomic snapshot of the dislocation density in the ordered GBs and 100 pct AIFs specimens in Figures 9(a through c) and (d through f), respectively. The partial dislocations are distributed throughout the grains in the specimen with ordered GBs. And as discussed previously, the dislocation density is also evidently higher due to the higher number of dislocation tangles and loops (refer Figures 9(a through c)). On the other hand, 100 pct AIFs have confined the dislocations mostly to the grains near the surface of the specimen (refer Figure 9(d through f)). Moreover, few of the dislocation loops that are evolved in the interior grains are annihilated by propagating toward the AIF region. Specifically considering the dislocation storage, the presence of AIF aids in the annihilation of the dislocations as the amorphous region has a higher FV and can accommodate the defects (such as dislocations).[25] Due to this phenomenon, the dislocation storage is lower after the deformation, but this does not necessarily mean that fewer dislocations have moved through the system and provided plastic strain accommodation. Efficient absorption of dislocations can delay crack nucleation at GBs.[25] On the other hand, the dislocation density in specimen with ordered GBs is high during the rolling process and leads to the formation of dislocation tangles and loops, which are primarily sessile in nature, leading to work hardening. While work hardening is helpful in delaying necking, most NC metals fail in a very brittle fashion due to premature crack nucleation and growth. Hence, it can be said that the presence of

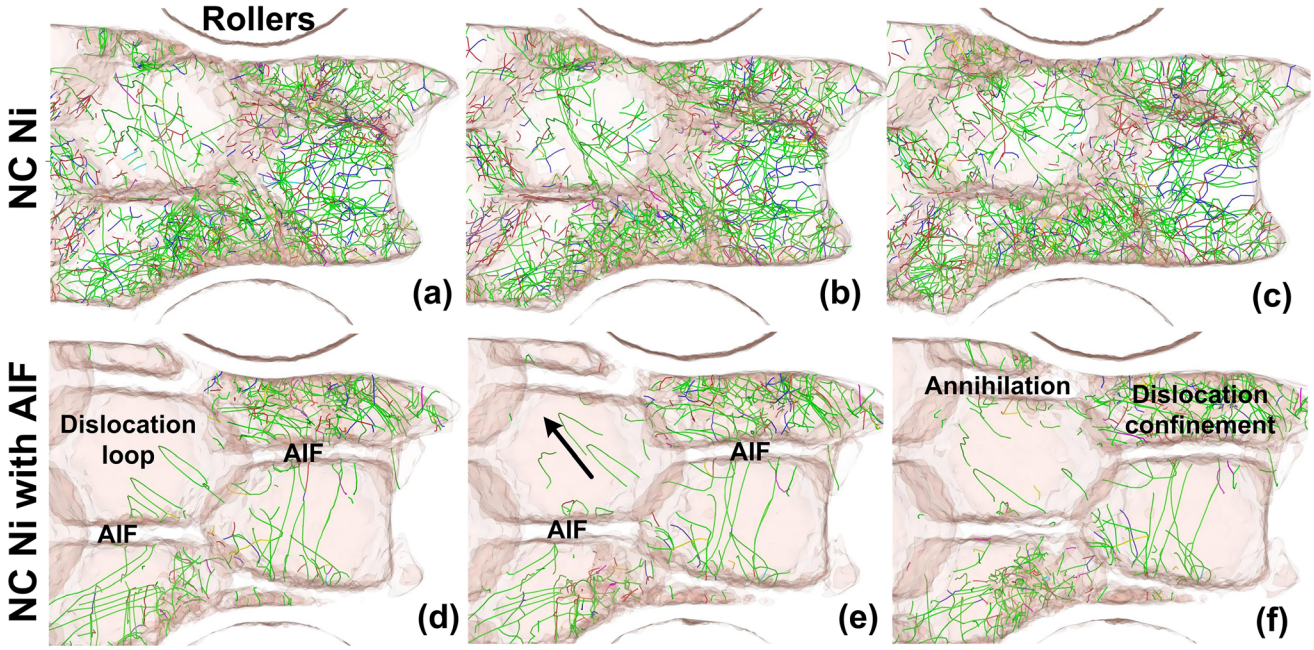

Fig. 9—Atomic snapshots illustrating the dislocation evolution during rolling process in NC Ni specimens with (*a* through *c*) ordered GBs and (*d* through *f*) 100 pct AIFs. The atoms have been omitted to observe the dislocation evolution and propagation efficiently.

AIF would actually improve the ductility of the specimen, for which there is now experimental evidence.[50] Moreover, under extreme deformation conditions, twinning is the mode of plastic deformation that aids in accumulating the strain in the specimen. Of the three specimens, the 100 pct AIF shows the lowest TB fraction at all three roller sets, whereas the ordered GBs show the highest TB fraction.

IV. CONCLUSIONS

In the present MD simulation-based study, we have performed the cold-rolling process on NC Ni specimens with different interfacial structures. We have considered an ordered GB network, an interface network with 50 pct AIFs, and a network with 100 pct AIFs. We have analyzed the effect of AIFs on the structural and texture evolution occurring in the specimens during the cold-rolling process. Based on the findings, we have drawn the following conclusions:

1. Grain orientation angle analysis has revealed that the distribution of the rolled specimen with ordered GBs changes non-uniformly with two larger peaks, which attributes to the stress-induced grain growth. However, the intensity of larger peaks reduces substantially with the inclusion of 50 pct AIF as the interface. For the rolled specimen with 100 pct AIF, the orientation angle distribution is uniform, and grain growth is limited.
2. The orientation analysis has shown that the severe plastic deformation in specimen with ordered GBs results in the RD-splitting, although few grains have retained their original orientation. In the case of the specimen with 100 pct AIFs, we find that the interface does not allow boundary movement or grain growth, and a higher number of grains have retained their initial orientation. Quantitative analysis has also shown that the specimen with AIFs can restrict the grain rotation or texture in the specimen.
3. Atomic stress distribution reveals that the rolled specimen with ordered GBs has an overall compressive residual stress. It is found that the average compressive stress in the grain interior is minimal, whereas the GB network shows higher compressive stress after cold-rolling, which might be responsible for the GB migration and subsequent grain growth. In the case of the rolled specimen with 100 pct AIFs, the rise in the compressive stress is lower than the specimen with ordered GBs due to uniform distribution of stress. Moreover, average positive stress in the grain interior is observed due to the anisotropic grain elongation without significant grain growth.
4. Dislocation analysis shows that the specimen with ordered GBs has the highest and uniform dislocation density, whereas the specimen with AIFs has a lower dislocation density due to dislocation annihilation at the interface. Moreover, it is found that a large number of dislocations are confined near the surface region in the specimens with AIF, which can aid in stress-induced strength at the surface and a softer core at the center.
5. In case of twinning, out of the three specimens, the 100 pct AIF sample shows the least fraction of the twins after passing through all three roller sets whereas the ordered GBs show the highest TB fraction.

Overall, it is found that the plastic deformation during the rolling of the specimen with ordered GBs occur through stress-induced grain growth (change in the grain sizes) and alteration in the grain orientations. On the other hand, the presence of AIFs aids in the plastic strain accumulation. Moreover, additional strain accretion in the specimen with AIFs occurs through a secondary mode of plastic deformation, *i.e.*, twinning mechanism. We believe that the present work can provide useful insights into the atomistic deformation mechanism of the NC materials with AIF during severe plastic deformation/material processing.

ACKNOWLEDGMENTS

The authors acknowledge the help provided by the Computer Centre of the National Institute of Technology Rourkela by providing the High-Performance Computing Facility (HPCF), which was essential for executing this work.

CONFLICT OF INTEREST

On behalf of all authors, the corresponding author states that there is no conflict of interest.

SUPPLEMENTARY INFORMATION

The online version of this article (https://doi.org/10.1007/s11661-021-06574-1) contains supplementary material, which is available to authorized users.

REFERENCES

1. M.A. Meyers, A. Mishra, and D.J. Benson: *Prog. Mater. Sci.*, 2006, vol. 51, pp. 427–556.
2. M. Dao, L. Lu, R.J. Asaro, J.T.M. De Hosson, and E. Ma: *Acta Mater.*, 2007, vol. 55, pp. 4041–65.
3. K.S. Kumar, H. Van Swygenhoven, and S. Suresh: *Acta Mater.*, 2003, vol. 51, pp. 5743–74.
4. V. Turlo and T.J. Rupert: *Acta Mater.*, 2018, vol. 151, pp. 100–11.
5. T.J. Rupert, W. Cai, and C.A. Schuh: *Wear*, 2013, vol. 298, pp. 120–26.
6. R. Rementeria, M.M. Aranda, C. Garcia-Mateo, and F.G. Caballero: *Mater. Sci. Technol.*, 2016, vol. 32, pp. 308–12.
7. T.J. Rupert and C.A. Schuh: *Acta Mater.*, 2010, vol. 58, pp. 4137–48.

8. H.V. Atkinson: *Acta Metall.*, 1988, vol. 36, pp. 469–91.
9. D.S. Gianola, S. Van Petegem, M. Legros, S. Brandstetter, H. Van Swygenhoven, and K.J. Hemker: *Acta Mater.*, 2006, vol. 54, pp. 2253–63.
10. L. Lu, M.L. Sui, and K. Lu: *Acta Mater.*, 2001, vol. 49, pp. 4127–34.
11. L. Li, T. Ungár, Y.D. Wang, G.J. Fan, Y.L. Yang, N. Jia, Y. Ren, G. Tichy, J. Lendvai, H. Choo, and P.K. Liaw: *Scripta Mater.*, 2009, vol. 60, pp. 317–20.
12. L. Li, T. Ungár, L.S. Toth, W. Skrotzki, Y.D. Wang, Y. Ren, H. Choo, Z. Fogarassy, X.T. Zhou, and P.K. Liaw: *Metall. Mater. Trans. A*, 2016, vol. 47A, pp. 6632–44.
13. K. Adam, D. Zöllner, and D.P. Field: *Model. Simul. Mater. Sci. Eng.*, 2018, vol. 26, p. 035011.
14. K.V. Reddy and S. Pal: *JOM*, 2020, vol. 72, pp. 3977–86.
15. H.A. Murdoch and C.A. Schuh: *J. Mater. Res.*, 2013, vol. 28, pp. 2154–63.
16. J.R. Trelewicz and C.A. Schuh: *Phys. Rev. B*, 2009, vol. 79, p. 094112.
17. A.J. Detor and C.A. Schuh: *Acta Mater.*, 2007, vol. 55, pp. 4221–32.
18. K.V. Reddy and S. Pal: *Trans. Indian Inst. Met.*, 2018, vol. 71, pp. 1721–34.
19. R. Kirchheim: *Acta Mater.*, 2002, vol. 50, pp. 413–19.
20. J. Wang, R. Janisch, G.K. Madsen, and R. Drautz: *Acta Mater.*, 2016, vol. 115, pp. 259–68.
21. F. Tang, D.S. Gianola, M.P. Moody, K.J. Hemker, and J.M. Cairney: *Acta Mater.*, 2012, vol. 60, pp. 1038–47.
22. W. Sigle, G. Richter, M. Rühle, and S. Schmidt: *Appl. Phys. Lett.*, 2006, vol. 89, p. 121911.
23. D. Foley and G.J. Tucker: *Model. Simul. Mater. Sci. Eng.*, 2016, vol. 24, p. 075011.
24. X. Shi and J. Luo: *Appl. Phys. Lett.*, 2009, vol. 94, p. 251908.
25. Z. Pan and T.J. Rupert: *Acta Mater.*, 2015, vol. 89, pp. 205–14.
26. C.M. Grigorian and T.J. Rupert: *Acta Mater.*, 2019, vol. 179, pp. 172–82.
27. S. Pal, K.V. Reddy, and C. Deng: *Comput. Mater. Sci.*, 2019, vol. 169, p. 109122.
28. J.D. Schuler and T.J. Rupert: *Acta Mater.*, 2017, vol. 140, pp. 196–205.
29. J.E. Ludy and T.J. Rupert: *Scripta Mater.*, 2016, vol. 110, pp. 37–40.
30. S.N. Mathaudhu: *Metall. Mater. Trans. A*, 2020, vol. 51A, pp. 6020–44.
31. A. Devaraj, W. Wang, R. Vemuri, L. Kovarik, X. Jiang, M. Bowden, J.R. Trelewicz, S. Mathaudhu, and A. Rohatgi: *Acta Mater.*, 2019, vol. 165, pp. 698–708.
32. A. Kulovits, S.X. Mao, and J.M.K. Wiezorek: *Acta Mater.*, 2008, vol. 56, pp. 4836–45.
33. H.T. Ni and X.Y. Zhang: *Philos. Mag. Lett.*, 2012, vol. 92, pp. 202–10.
34. K.V. Reddy and S. Pal: *Comput. Mater. Sci.*, 2020, vol. 184, p. 109935.
35. K.V. Reddy and S. Pal: *J. Appl. Phys.*, 2020, vol. 127, p. 154305.
36. K.V. Reddy and S. Pal: *J. Appl. Phys.*, 2019, vol. 125, p. 095101.
37. K.V. Reddy and S. Pal: *Steel Res. Int.*, 2019, vol. 90, p. 1800636.
38. K.V. Reddy and S. Pal: *J. Mol. Model.*, 2021, vol. 27, pp. 1–8.
39. P. Hirel: *Comput. Phys. Commun.*, 2015, vol. 197, pp. 212–19.
40. S. Plimpton: *J. Comput. Phys.*, 1995, vol. 117, pp. 1–19.
41. P.M. Larsen, S. Schmidt, and J. Schiøtz: *Model. Simul. Mater. Sci. Eng.*, 2016, vol. 24, p. 055007.
42. D.J. Evans and B.L. Holian: *J. Chem. Phys.*, 1985, vol. 83, pp. 4069–74.
43. A. Stukowski: *Model. Simul. Mater. Sci. Eng.*, 2009, vol. 18, p. 015012.
44. R. Krakow, R.J. Bennett, D.N. Johnstone, Z. Vukmanovic, W. Solano-Alvarez, S.J. Lainé, J.F. Einsle, P.A. Midgley, C.M.F. Rae, and R. Hielscher: *Proc. R. Soc. A*, 2017, vol. 473, p. 20170274.
45. Y.B. Zhang, A. Godfrey, Q. Liu, W. Liu, and D.J. Jensen: *Acta Mater.*, 2009, vol. 57, pp. 2631–39.
46. G. Faraji, H.S. Kim, and H.T. Kashi: *Severe Plastic Deformation: Methods, Processing and Properties*, Elsevier, Amsterdam, 2018.
47. N.S. Lee, J.H. Chen, P.W. Kao, L.W. Chang, T.Y. Tseng, and J.R. Su: *Scripta Mater.*, 2009, vol. 60, pp. 340–43.
48. H.W. Huang, Z.B. Wang, J. Lu, and K. Lu: *Acta Mater.*, 2015, vol. 87, pp. 150–60.
49. X. Zhou, Y. Liu, G.E. Thompson, G.M. Scamans, P. Skeldon, and J.A. Hunter: *Metall. Mater. Trans. A*, 2011, vol. 42A, pp. 1373–85.
50. J.L. Wardini, C.M. Grigorian, and T.J. Rupert: *Materials*, 2021, vol. 17, p. 101134.